Analysis of an eddy-current brake considering finite radius and induced magnetic flux

Kapjin Lee and Kyihwan Park

View Online   Export Citation

ARTICLES YOU MAY BE INTERESTED IN

AIP
Publishing

Analysis of an eddy-current brake considering finite radius and induced magnetic flux

Kapjin Lee[a] and Kyihwan Park[b]
Department of Mechatronics, Kwangju Institute of Science and Technology (K-JIST), 1 Oryong-dong, Buk-gu, Kwangju 500-712, Republic of Korea

Since the eddy-current problem usually depends on the geometry of the moving conductive sheet and the pole shape, there is no general method to find an analytical solution. The analysis of the eddy currents in a rotating disk with an electromagnet is performed in the case of time-invariant field with the consideration of the boundary conditions of the rotating disk and induced magnetic flux. First, the concept of Coulomb's law and the method of images are introduced with the consideration of the boundary conditions. Second, the induced magnetic flux density is calculated by using Ampere's law. Third, the net magnetic flux density is introduced by defining the *magnetic Reynolds number R_m* as the ratio of the induced magnetic flux density to the applied magnetic flux density. Finally, the braking torque is calculated by applying the Lorentz force law and the computed results are compared with experimental ones. © *2002 American Institute of Physics.* [DOI: 10.1063/1.1510593]

I. INTRODUCTION

When a time-invariant magnetic flux penetrates moving conductive sheet, eddy currents are induced around the pole projection area. The eddy currents produce an induced magnetic flux, which reduces the net magnetic flux passing through the moving conductive sheet. The induced magnetic flux is much smaller than the applied magnetic flux in the low velocity region. As the velocity increases, however, the induced magnetic flux increases. According to the Lorentz force law, a braking torque is generated by the interaction between the eddy currents and net magnetic flux. In the low velocity region, the braking torque increases as the velocity increases. In the high velocity region, however, the braking torque reaches a saturation level due to the reduced net magnetic flux. Many analytical methods have been used to model the eddy current distribution and braking torque.[1–8]

Schieber[1–3] presented an analytical method based on the governing equation of magnetic vector potential with the assumption that the induced magnetic flux is negligible in the low velocity region. To identify the boundary of the velocity region, he introduced the *magnetic Reynolds number R_m* which is expressed as the induced magnetic flux density over the applied magnetic flux density from an electromagnet: When the *magnetic Reynolds number R_m* is lower than unity, the induced magnetic flux may be ignored. His model showed linearly increasing braking torque in the high velocity region. In 1987, Wiederick *et al.*[4] suggested a lumped method with an additional assumption that the eddy currents are uniform inside the rectangular pole projection area as long as the velocity of the translating sheet is constant. They obtained the electromotive force across the pole projection area from the motional induced electric field due to the mov-

ing media, $\mathbf{v} \times \mathbf{B}$. The volume inside and outside of the pole projection were modeled as equivalent internal and external resistances, respectively. By using the electromotive force and equivalent resistances, they could obtain the eddy-current density in a lumped way based on Ohm's law. In 1988, Heald[5] derived the surface charge density at the edge of the pole projection area and calculated the nonuniform electric field intensity by using Coulomb's law, with the assumption that the width of the moving conductive sheet is infinite.

There were analytical methods in which the induced magnetic flux was considered. The paper presented by Smythe[6] in 1942 showed that the estimated braking torque agreed well with the experimental one in the low velocity region, but did not agree well in the high velocity region. The asymptotic behavior showed that the braking torque fell off more rapidly than the inverse of the velocity in the high velocity region, which is in contradiction with experimental results. In 1991, Wouterse[7] assumed that the braking torque was proportional to the inverse of the velocity in the high velocity region and that the power dissipation is constant at infinite speed. Based on the experimental results, he obtained the critical speed at which the exerted force is maximum and the maximum force, described by the air gap and equivalent pole diameter. In 1992, Salow[8] used the Maxwell recession velocity in order to consider the induced magnetic flux, with the assumption that the conductive sheet is infinite.

The methods proposed by these authors[1–8] were successful but had various failings: Some results could not show the asymptotic behavior for the high velocity region. Others did not take the boundary condition or nonuniform eddy-current distribution into account. In this article, the analysis of the eddy-current density distribution and the braking torque are presented for a rotating disk which has a finite radius. The boundary condition of the finite radial length is considered by using the mapping technique and the method of images.

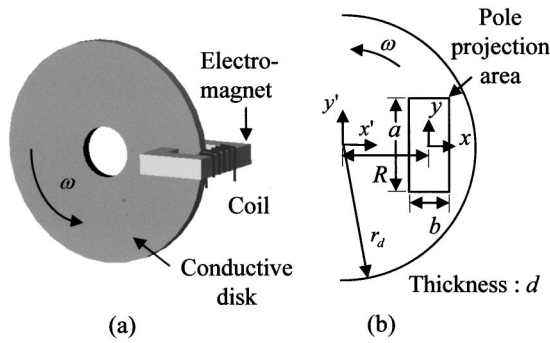[a]Electronic mail: kap@kjist.ac.kr
[b]Electronic mail: khpark@kjist.ac.kr

FIG. 1. Configuration of the rotating conductive disk and electromagnet: (a) bird's-eye view and (b) cross section view.

FIG. 2. Representation of the position and velocity vectors at P.

II. ANALYSIS OF EDDY CURRENTS

A. Eddy currents for disk of infinite radius

Figure 1 shows a rotating conductive disk in which we analyze the eddy currents. a and b are the width and radial length of the rectangular pole of the electromagnet. r_d, R, and d are the radius of the disk, distance to the pole center from the center of the disk, and thickness of the disk, respectively. A direct current is applied to the coil wound around the electromagnet to produce a constant magnetic flux density $\mathbf{B}$ through the pole projection area. The conductive disk rotates at a constant angular velocity ω in the counterclockwise direction. All the unprimed variables are represented in the fixed frame (xy coordinate) located at the center of the pole projection area. All of the primed variables are represented in the moving frame ($x'y'$ coordinate) attached to the center of the rotating disk.

$\mathbf{r}$ and $\mathbf{r}'$ are the displacement vectors to the point P from the fixed frame and the moving frame centers as shown in Fig. 2, respectively. $\mathbf{v}$ is the velocity vector at the point P with respect to the moving frame and its magnitude is expressed as $r'\omega$. From Fig. 2, by using the geometrical relations $y = r' \sin \phi'$ and $R + x = r' \cos \phi'$, the velocity components of v_x and v_y in the fixed frame are, respectively,

$$v_x = v \sin \phi' = \omega r' \sin \phi' = \omega y, \tag{1}$$

$$v_y = v \cos \phi' = \omega r' \cos \phi' = \omega(R + x). \tag{2}$$

$\mathbf{v}$ is represented by $-v_x \mathbf{i} + v_y \mathbf{j}$, where $\mathbf{i}$ and $\mathbf{j}$ are the unit vectors in the x and y directions, respectively.

From a microscopic point of view,[9] the movable charges q are expected to collect at the edges of the pole projection area due to the magnetic force $q\mathbf{v} \times \mathbf{B}$. This magnetic force leads to a separation of charges, which produces an electric field $\mathbf{E}$. The eddy-current density $\mathbf{J}$ induced in the disk in the fixed frame can be obtained as[5]

$$\mathbf{J}' = \sigma(\mathbf{E} + \mathbf{v} \times \mathbf{B}), \tag{3}$$

where σ is the conductivity of the disk.

Let us consider how $\mathbf{E}$ of Eq. (3) is expressed. The first step is to find the charges. The charges collected at the ends of the volume of the pole projection are analogously calculated by using the method of calculating the magnetic pole density at the surface of a permanent magnet:[10] The magnetic

From the analytical results, it is shown that the eddy currents are not uniform inside the pole projection area, even though the angular velocity of the disk is constant. Also, in order to present a valid asymptotic behavior, the induced magnetic flux density is calculated in a lumped way by using Ampere's law.

In the first step, the eddy-current density in the rotating disk is obtained from the surface charges generated at the end of the pole projection area due to the motional induced electric field $\mathbf{v} \times \mathbf{B}$ with the assumption that the rotating disk radius is infinite.[5] The movable charges q are subject to the magnetic force $q\mathbf{v} \times \mathbf{B}$ that will lead to a separation of the charges: The positive ones being forced to move in the direction of $\mathbf{v} \times \mathbf{B}$ and the negative ones in the opposite direction. From the charges, the electric field intensity $\mathbf{E}$ is obtained by using Coulomb's law.

In the second step, the finite disk radius is considered by introducing a fictitious charge configuration, based on the method of images,[9] so that the imaginary electric-field intensity due to the fictitious charge configuration could satisfy the boundary condition that the radial component of the eddy currents is zero at the edge of the rotating disk. To obtain the imaginary electric-field intensity, the primary electric-field intensity due to the surface charges is transformed by using the mapping method. Then, the imaginary electric-field intensity is obtained by using the method of images. By summing the primary and imaginary electric-field intensities, we can obtain the net electric-field intensity which satisfies the boundary condition.

In the third step, the induced magnetic flux density is calculated in a lumped way. The radial component of the eddy-current density is integrated numerically to obtain the eddy current. From the net eddy current, the induced magnetic flux density is calculated by using Ampere's law.

In the fourth step, the net magnetic flux density is expressed by using an exponential function that is satisfied in the two extreme cases in which the net magnetic flux density equals to the applied magnetic flux and zero, when the angular velocity is zero and infinite, respectively.[7]

Finally, by using the Lorentz force law,[11] the braking torque is numerically calculated and the results are compared with the experiment.
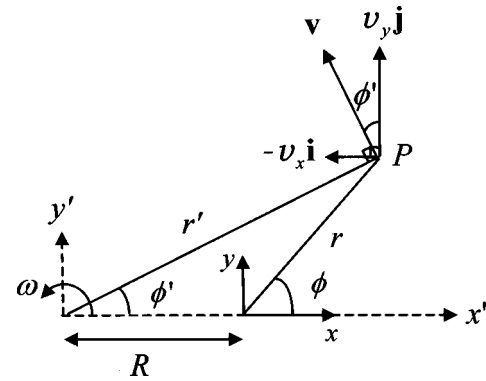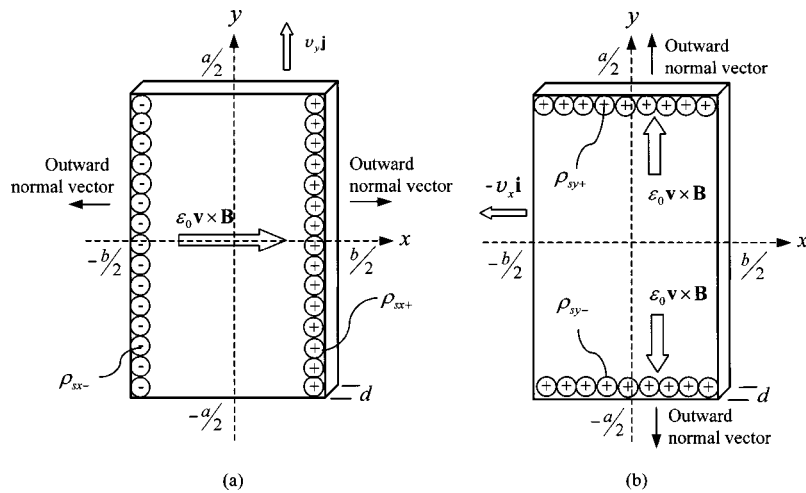
FIG. 3. The surface charge distributions obtained by using the polarization for: (a) y directional motion and (b) x directional motion.

(a)   (b)

pole density is defined as the inner product of the magnetization and the unit outward normal vector. Based on this analogy, the surface charge density is also obtained as the inner product of the polarization ($=\epsilon_0 \mathbf{v} \times \mathbf{B}$) and the unit outward normal vector.

The rotating motion of the disk can be equivalently considered as having the translational velocities as shown in Fig. 3. The polarization and the unit outward normal vector can be considered for each translational velocity, respectively. When $\rho_{sx\pm}$ and $\rho_{sy\pm}$ are defined as the surface charge densities on the planes parallel to the yz plane at $x = \pm b/2$ and the xz plane at $y = \pm a/2$ respectively, they are written as follows[5]

$$\rho_{sx+} = \epsilon_0 \omega (R + b/2) B_z, \tag{4}$$

$$\rho_{sx-} = -\epsilon_0 \omega (R - b/2) B_z, \tag{5}$$

$$\rho_{sy+} = \epsilon_0 \omega a/2 B_z, \tag{6}$$

$$\rho_{sy-} = \epsilon_0 \omega a/2 B_z, \tag{7}$$

where B_z is the z component of $\mathbf{B}$.

Finally, the electric-field intensity $\mathbf{E}$ is represented by $\mathbf{E} = E_x \mathbf{i} + E_y \mathbf{j}$, where E_x and E_y are obtained by using Coulomb's law[11]

$$
\begin{aligned}
E_x = \frac{\omega B_z}{4\pi}\Bigg[& -(2R+b)\tan^{-1}\frac{2y-a}{2x-b} + (2R-b)\tan^{-1} \\
& \times\frac{2y-a}{2x+b} + (2R+b)\tan^{-1}\frac{2y+a}{2x-b} - (2R-b)\tan^{-1} \\
& \times\frac{2y+a}{2x+b} \\
& + \frac{a}{2}\ \ln\frac{\{(2x+b)^2+(2y-a)^2\}\{(2x+b)^2+(2y+a)^2\}}{\{(2x-b)^2+(2y-a)^2\}\{(2x-b)^2+(2y+a)^2\}}\Bigg],
\end{aligned}
\tag{8}
$$

$$
E_y = -\frac{\omega B_z}{8\pi}\Bigg[b\ln\frac{\{(2x-b)^2+(2y-a)^2\}\{(2x+b)^2+(2y-a)^2\}}{\{(2x-b)^2+(2y+a)^2\}\{(2x+b)^2+(2y+a)^2\}} + 2R\ln\frac{\{(2x-b)^2+(2y-a)^2\}\{(2x+b)^2+(2y+a)^2\}}{\{(2x+b)^2+(2y-a)^2\}\{(2x-b)^2+(2y+a)^2\}} \\
+ 2a\left(\tan^{-1}\frac{2x+b}{2y-a} + \tan^{-1}\frac{2x+b}{2y+a} - \tan^{-1}\frac{2x-b}{2y-a} - \tan^{-1}\frac{2x-b}{2y+a} \right) \Bigg].
\tag{9}
$$

Since the electric-field intensity is specified, the eddy current density $\mathbf{J}'$ (same as $\mathbf{J}$) induced in the disk in the moving frame can be obtained from Eq. (3). Therefore, the eddy-current densities inside the pole projection area are finally expressed in x and y components as

$$J_x = \sigma(E_x + \omega(R+x)B_z), \tag{10}$$

$$J_y = \sigma(E_y + \omega y B_z). \tag{11}$$

Since B_z is zero outside the pole projection area, the eddy-current density outside the pole projection area is represented simply by $\mathbf{J} = \sigma \mathbf{E}$.

This analysis is performed under the assumption that the disk radius is infinite, which is not true in real applications. When the disk has a finite radius, a boundary condition is that the radial component of the eddy current is zero at the edge of the disk. In order to indicate that the electric-field intensities E_x and E_y of Eqs. (8) and (9), respectively, are obtained without considering this boundary condition, they are denoted by $E_x^{(p)}$ and $E_y^{(p)}$, called the primary electric-
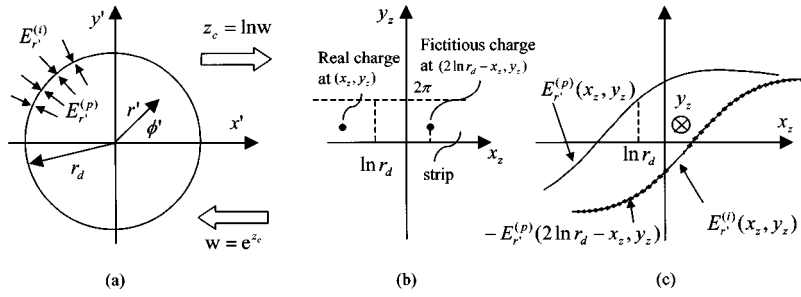
FIG. 4. Representation of the relation between (a) w plane and (b) z_c plane, and (c) $E_{r'}^{(p)}$ and $E_{r'}^{(i)}$.

field intensities in the x and y directions, respectively. Therefore, we should impose the requirement of the boundary condition on the aforementioned result.

B. Eddy currents with consideration of boundary condition

First, the work space is transformed to the cylindrical coordinate space as shown in Fig. 4(a) and mapped onto the z_c plane as shown in Fig. 4(b), to use the method of images in the z_c plane. Since $x' = r' \cos \phi'$ and $y' = r' \sin \phi'$ from Fig. 2, the relations between the fixed Cartesian coordinate (x,y) and the moving cylindrical coordinate (r',ϕ') are

$$x = x' - R = r' \cos \phi' - R, \tag{12}$$

$$y = y' = r' \sin \phi'. \tag{13}$$

By transforming Eqs. (8) and (9) to the moving cylindrical coordinates, and using Eqs. (12) and (13), the radial component of the primary electric field intensity $E_{r'}^{(p)}$ can be expressed as

$$E_{r'}^{(p)}(r',\phi') = E_{x'}^{(p)} \cos \phi' + E_{y'}^{(p)} \sin \phi'. \tag{14}$$

Since the cylindrical coordinate space can be expressed by using the complex variable w as

$$w = r' e^{i\phi'}, \tag{15}$$

z_c defined as $\ln w$ is represented as follows

$$z_c = \ln w = \ln r' + \phi' i = x_z + y_z i. \tag{16}$$

From Eq. (16), it is known that all the points, $0 \leq r' \leq r_d$ and $0 \leq \phi' \leq 2\pi$, in Fig. 4(a) are mapped onto the region, $x_z \leq \ln r_d$ and $0 \leq y_z \leq 2\pi$ as shown in Fig. 4(b).

The key insight to consider the boundary condition is based on the method of images.[9] It is assumed that there exist fictitious charges in the nonshaded area which produce an imaginary electric-field intensity $E^{(i)}$ and satisfy the boundary condition expressed as

$$J_{r'} = \sigma E_{r'} = \sigma(E_{r'}^{(p)} + E_{r'}^{(i)}) = 0 \quad \text{at } x_z = \ln r_d. \tag{17}$$

Clearly, this will always be satisfied if the fictitious charges have the same magnitude as the real charges and are located at the symmetric position about $x_z = \ln r_d$. Therefore, the relation between $E_{r'}^{(p)}$ and $E_{r'}^{(i)}$ can be derived from the symmetric configuration between the real charges and the fictitious charges as

$$E_{r'}^{(i)}(x_z,y_z) = -E_{r'}^{(p)}(2 \ln r_d - x_z, y_z), \tag{18}$$

which is represented graphically in Fig. 4(c).

Mapping the point $(2 \ln r_d - x_z, y_z)$ which is the position of the fictitious charges again onto the w plane by using Eq. (16) to deal with the problem in the w plane, we have the relation

$$w = \frac{r_d^2}{r'} e^{i\phi'}. \tag{19}$$

By using Eqs. (18) and (19), therefore, we have the relation

$$E_{r'}^{(i)}(r',\phi') = -E_{r'}^{(p)}\left(\frac{r_d^2}{r'},\phi'\right). \tag{20}$$

Since $E_{r'} = E_{r'}^{(p)} + E_{r'}^{(i)}$, from Eqs. (10)–(13) and the transformation of the coordinate, the radial component of the eddy-current density $J_{r'}$ in the disk finally has the form

$$J_{r'}(r',\phi') = \sigma\left\{ E_{r'}^{(p)}(r',\phi') - E_{r'}^{(p)}\left(\frac{r_d^2}{r'},\phi'\right) \right.$$
$$\left. + \omega r' \cos^2 \phi' B_z + \omega r' \sin^2 \phi' B_z \right\}, \tag{21}$$

$$J_{r'}(r',\phi') = \sigma\left\{ E_{r'}^{(p)}(r',\phi') - E_{r'}^{(p)}\left(\frac{r_d^2}{r'},\phi'\right) \right\}, \tag{22}$$

inside and outside the pole projection area, respectively. The mathematical expressions of Eqs. (21) and (22) are not simple, but can be obtained straightforwardly. Since $E_{r'}^{(p)}$ is proportional to ωB_z, it is clear that Jr' inside the pole projection area is proportional to ωB_z from Eq. (21). The average eddy-current density J_{avg} inside the pole projection area, therefore, can be modified as follows

$$J_{\text{avg}} = \frac{\int_s J_{r'} ds}{ab B_z \omega} B_z \omega = C_{\text{norm}} B_z \omega. \tag{23}$$

Since C_{norm} is a function of only the geometric parameters listed in Table I, it can be said that the average eddy-current density is proportional to the applied magnetic flux density and the angular velocity of the disk.

Figures 5(a)–5(c) show the radial components of the eddy-current density distributions due to the primary, imaginary, and net electric-field intensities, respectively. All the physical parameters are listed in Table I, except setting $a = 40$ mm in order to magnify the effect that the eddy currents tend to concentrate toward the edge of the y direction in the rectangular pole projection area. It is expected that the magnitude of each distribution increases without changing its shape as ωB_z increases.
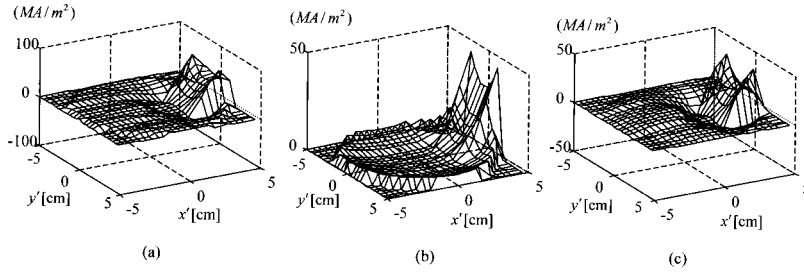
FIG. 5. The eddy-current density distributions due to (a) the primary electric-field intensity, (b) the imaginary electric-field intensity, and (c) the net electric-field intensity.

C. Eddy currents with consideration of induced magnetic flux

The preceding analysis is performed by ignoring the induced magnetic flux caused by the eddy current. As the angular velocity increases, the induced magnetic flux increases. Since the induced magnetic flux flows in the opposite direction to the applied magnetic flux, the net magnetic flux is reduced. For an accurate result in the high angular velocity region, the net magnetic flux density B_Z is obtained in a lumped way, instead of solving a magnetic diffusion equation. Actually, it is very difficult to solve the magnetic diffusion equation.

The induced magnetic flux density is calculated from the eddy-current density by using Ampere's law.[11] Since the tangential component of the eddy-current density is expected to be smaller than the radial one in the pole projection area, it is ignored for simplicity in considering the induced magnetic flux. The schematic diagram to calculate the induced magnetic flux density is represented in Fig. 6. The radial component of the eddy current $I_{r'}$ expressed in a lumped way in the pole projection area is obtained simply from Eq. (23) as follows

$$I_{r'} = a d C_{\text{norm}} B_z \omega. \tag{24}$$

Then, by assuming the induced magnetic flux intensity H_i in the electromagnet is zero, Ampere's law for the contour c_a in Fig. 6(b) can be expressed as

$$2 l_g H_i = I_{r'}. \tag{25}$$

Therefore, the induced magnetic flux B_i has the form of

$$B_i = \frac{a d \mu_0 C_{\text{norm}}}{2 l_g} B_z \omega = \gamma B_z \omega. \tag{26}$$

Simply, the net magnetic flux density $\mathbf{B_Z}$ can be considered as the summation of the applied and the induced magnetic fluxes in a vector form as

$$\mathbf{B_Z} = \mathbf{B_z} + \mathbf{B_i}. \tag{27}$$

Figure 7 shows the simplified distributions of the magnetic flux density. When the angular velocity of the disk ω is zero, the net magnetic flux density distribution B_Z is the same as B_z since $B_i = 0$. As ω increases, however, the distribution of B_Z looks like the one in Fig. 7(b) due to the induced magnetic flux B_i. In the left-hand side of the location where the eddy currents is represented as $I_{r'}$, B_Z is increased since B_i is added to B_z. On the other hand, B_Z is decreased since B_i is subtracted from B_z. As ω increases, there is an angular velocity ω_m at which the density difference between the sides reaches a maximum, as shown in Fig. 7(c). This occurs when $B_z = B_i$. Since the braking torque can be calculated as the derivative of the magnetic energy[12] stored in the air gap with respect to the rotating angle, it can be said that the maximum braking torque is exerted when $B_z = B_i$. above the angular velocity where the maximum force is exerted, however, B_Z in the right-hand side goes to a negative value, which is not consistent with the asymptotic behavior of the net magnetic flux density.[7] To avoid such a conflict, the net magnetic flux density B_Z is assumed to have the form as follows

$$B_Z = B_z e^{-\alpha R_m}, \tag{28}$$

where α is constant. Since the *magnetic Reynolds number* R_m[13] is defined as B_i / B_z, it is expressed using Eq. (26) as

TABLE I. Parameters.

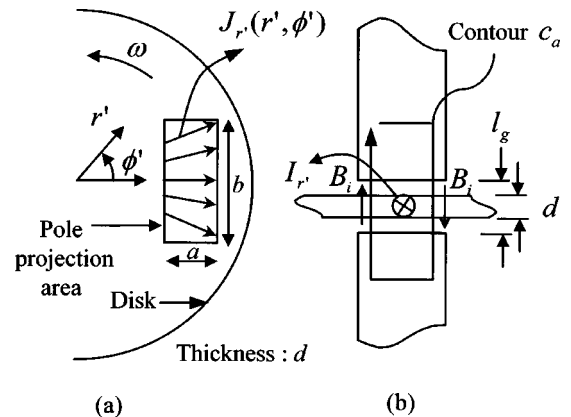| Description	Variable	Value	Unit
Width of the pole	a	20	mm
Height of the pole	b	20	mm
Air gap	l_g	5	mm
Radius of the disk	r_d	50	mm
Thickness of the disk	d	3	mm
Pole location	R	32.3	mm
Conductivity of the disk	σ	5.79×10^7	$\frac{1}{\Omega m}$
Flux density in the air gap	B_z	0.3	T

FIG. 6. The schematic diagram to calculate the induced magnetic flux density: (a) the radial component of the net eddy-current density $J_{r'}$ (b) Ampere's law for the contour c_a.

FIG. 7. Simplified magnetic flux densities of B_z, B_i, and B_Z when (a) ω = 0, (b) $\omega < \omega_m$, (c) $\omega = \omega_m$, and (d) $\omega > \omega_m$.

$$R_m = \frac{B_i}{B_z} = \gamma\omega. \tag{29}$$

From Eqs. (28) and (26), it is clear that the net magnetic flux density B_Z equals the applied magnetic flux density B_z when the angular velocity ω is zero and the net magnetic flux density B_Z goes to zero as ω becomes infinite. These two extreme cases agree well with the results of a thought experiment done in a previous study.[7]

Using the Lorentz force law,[11] we have the tangential force $F_{\phi'}$ in the volume under the pole projection area as follows.

$$\mathbf{F} = \int_V \mathbf{J} \times \mathbf{B} dV = F_{\phi'}\mathbf{a}_{\phi'} + F_{r'}\mathbf{a}_{r'}, \tag{30}$$

$$F_{\phi'} = -\int_V J_{r'} B_z e^{-\alpha\gamma\omega} dV, \tag{31}$$

where V is a total volume of the pole projection. Also, the braking torque has the form

$$\mathbf{T_b} = \mathbf{r'} \times \mathbf{F} = -dB_z e^{-\alpha\gamma\omega} \int_s r' J_{r'} ds \hat{\mathbf{k}}, \tag{32}$$

where s is the pole projection area. The braking torque can be simplified by using a normalized term as follows

$$\mathbf{T_b} = -\omega B_z^2 e^{-\alpha\gamma\omega} d \int_s \frac{r' J_{r'}}{\omega B_z} ds \hat{\mathbf{k}} = -t_{norm} B_z^2 \omega e^{-\alpha\gamma\omega} \hat{\mathbf{k}}. \tag{33}$$

Now we are faced with the problem of obtaining α. We assumed that the maximum force is exerted when $B_z = B_i$, that is when $R_m = 1$. From this assumption, the angular ve-
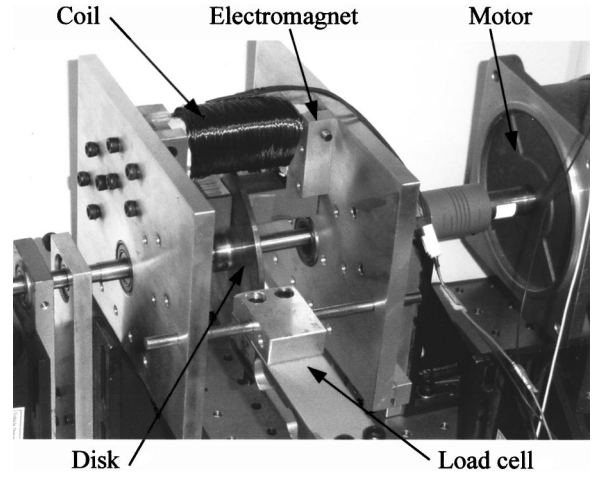
locity ω_m where the maximum torque is exerted is obtained as $1/\gamma$ from Eq. (29). Hence, we know the condition for the maximum braking torque at $\omega_m = 1/\gamma$ is

$$\left.\frac{\partial T_b}{\partial \omega}\right|_{\omega=\omega_m} = t_{norm} B_z^2 e^{-\alpha\gamma\omega_m}(\alpha\gamma\omega_m - 1)$$

$$= t_{norm} B_z^2 e^{-\alpha}(\alpha - 1) = 0. \tag{34}$$

Equation (34) always is satisfied if α is unity. Finally, T_b is obtained as

$$\mathbf{T_b} = -t_{norm} B_z^2 \omega e^{-\gamma\omega} \hat{\mathbf{k}}, \tag{35}$$

where γ and t_{norm} are obtained numerically. We can find out the braking torque for the various velocity and applied flux density. The computed results of the braking torque are compared with the experimental ones in Sec. III.

III. EXPERIMENTAL VALIDATION OF THE PROPOSED MODEL

To validate the accuracy of the proposed model, the braking torque is measured experimentally. The experimental setup in Fig. 8 is composed of a rotating disk, an electric motor, an electromagnet, and a load cell. The electric motor is used to rotate the disk with constant angular velocity. The electromagnet supplies the magnetic flux which penetrates the pole projection area in the disk. The braking torque is generated in the rotating disk and the reaction torque is exerted on the electromagnet. The reaction torque is translated to the load cell. As a result, the braking torque can be measured by reading the output voltage of the load cell.

Figure 9 shows the computed and measured braking torques versus the angular velocity of the disk for different magnetic flux densities in an electromagnet. The solid line represents the analytical results. "*, ○, +, and ×" represent the experimental results for $B = 0.2$ T, 0.25 T, 0.3 T, and 0.35 T, respectively. It is observed that the measured braking torques reach saturation levels at high angular velocities. As the angular velocity of the disk increases, the induced magnetic flux density increases due to the increasing eddy currents. Since the induced magnetic flux density decreases the
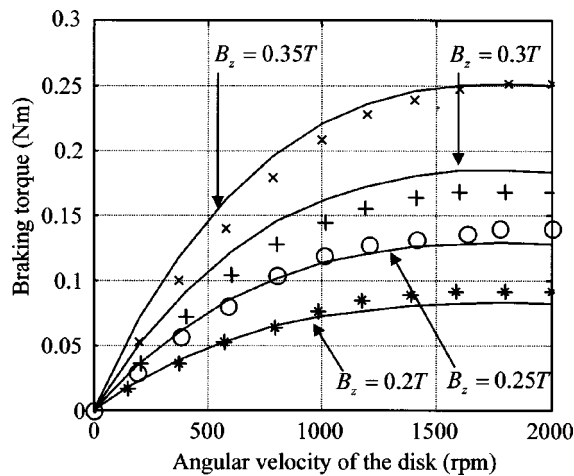

FIG. 8. Experimental setup.

FIG. 9. Comparison between the computed braking torques and experimental ones when the applied magnetic flux density B_z is 0.2 T, 0.25 T, 0.3 T, and 0.35 T, respectively.

net magnetic flux density passing through the pole projection area, the braking torque saturates as the angular velocity of the disk increases. It is also observed that the computed braking torques agree with the measured ones within 10%. One source of error is the temperature increase of the disk. A temperature increase of 10 °C leads to the conductivity decrease of 4% because the temperature coefficient of resistance of pure copper is about 4000 ppm/° C.[14] Actually, the temperature increase is less than 10 °C, when $B = 0.2$ T or $B = 0.25$ T, which means that the induced eddy currents are not enough to increase the temperature of the disk. However, when $B = 0.3$ T or $B = 0.35$ T, temperature increase is about 20 °C. Hence, it is observed that the measured braking torques becomes smaller than computed ones for the larger flux density. In spite of some error, it can be said that the proposed model presents fairly accurate results for both the low and high velocity regions in the eddy-current analysis of the system composed of the rotating disk and an electromagnet.

IV. CONCLUSIONS

The analyses of the eddy-current density distribution and the braking torque were presented for the rotating disk which had a finite radius. The proposed modeling method provides us with accurate results within 10%. On the other hand, the results tell us the limitation of the proposed modeling method: It is ignored that the conductivity of the copper is affected by the temperature variation. Also, the induced magnetic flux is considered in a lumped way. In spite of the limitation, the proposed model shows improvements in the points of view of that finite radius of the disk and the induced magnetic flux are considered.

ACKNOWLEDGMENTS

[1] D. Schieber, Proc. IEEE **119**, 1499 (1972).
[2] D. Schieber, Proc. IEEE **121**, 117 (1974).
[3] D. Schieber, *Electromagnetic Induction Phenomena*, Springer Series in Electrophysics Vol 16 (Springer, Berlin, 1986).
[4] H. D. Wiederick, N. Gauthier, D. A. Campbell, and P. Rochon, Am. J. Phys. **55**, 500 (1987).
[5] M. A. Heald, Am. J. Phys. **56**, 521 (1988).
[6] W. R. Smythe, Trans. AIEE **61**, 681 (1942).
[7] J. H. Wouterse, IEE. Proc. B **138**, 153 (1991).
[8] W. M. Saslow, Am. J. Phys. **60**, 693 (1992).
[9] R. K. Wangsness, *Electromagnetic Fields*, 2nd ed. (Wiley, New York, 1986), pp. 273–274.
[10] P. Lorrain and Dale R. Corson, *Electromagnetic Fields and Waves*, 2nd ed. (Freeman, San Francisco, 1970).
[11] W. H. Hayt, *Engineering Electromagnetics*, 5th ed. (McGraw–Hill, New York, 1989).
[12] H. H. Woodson and J. R. Melcher, *Electromechanical Dynamics Part I: Discrete Systems* (Krieger, Malabar, Florida, 1990).
[13] H. H. Woodson and J. R. Melcher, *Electromechanical Dynamics Part II: Fields, Forces, and Motion* (Krieger, Malabar, Florida, 1985).
[14] *ASM Handbook, Properties and Selection: Nonferrous Alloys and Special-Purpose Materials*, 10th ed. (ASM International, Materials Park, OH, 1990), Vol. 2, p. 823.